For a 0.5 μbar (5 μbar) atmosphere, electrons at initial energy ≳70 keV (≳300 keV) will penetrate to the satellite's surface. Precise estimates of the modifications of Triton's atmosphere and surface, including seasonal variations in the rates, will be reported later.

REFERENCES AND NOTES

1. S. M. Krimigis *et al.*, *Space Sci. Rev.* **21**, 329 (1977).
2. S. M. Krimigis, in *Comparative Study of Magnetospheric Systems* (Centre National d'Etudes Spatiales, Paris, 1986), p. 99.
3. N. F. Ness *et al.*, *Science*, **246**, 1473 (1989).
4. E. C. Stone and E. Miner, *ibid.*, p. 1417.
5. L. R. Lyons *et al.*, *J. Geophys. Res.* **93**, 12932 (1988).
6. S. M. Krimigis *et al.*, *Science* **212**, 225 (1981); S. M. Krimigis *et al.*, *ibid.* **215**, 571 (1982).
7. S. M. Krimigis *et al.*, *ibid.* **233**, 97 1986).
8. D. C. Hamilton *et al.*, *Geophys. Res. Lett.* **7**, 813 (1980).
9. G. L. Siscoe, *Icarus* **24**, 311 (1975).
10. A. F. Cheng, *J. Geophys. Res.* **92**, 15315 (1987).
11. J. W. Belcher *et al.*, *Science* **246**, 1478 (1989).
12. B. H. Mauk *et al.*, *J. Geophys. Res.* **92**, 15283 (1987).
13. M. F. Thomsen *et al.*, *ibid.* **82**, 5541 (1977).
14. A. F. Cheng *et al.*, *ibid.* **90**, 526 (1985).
15. F. M. Neubauer, *Adv. Space Res.*, in press.
16. A. L. Broadfoot *et al.*, *Science* **246**, 1459 (1989).
17. J. W. Warwick *et al.*, *ibid.*, p. 1498.
18. A. F. Cheng, *Geophys. Res. Lett.* **16**, 953 (1989).
19. D. A. Gurnett *et al.*, *Science* **246**, 1494 (1989).
20. R. D. Zwickl *et al.*, *J. Geophys. Res.* **88**, 125 (1981).
21. E. Kirsch *et al.*, *Geophys. Res. Lett.* **8**, 169 (1981); E. Kirsch *et al.*, *Nature* **292**, 718 (1981); A. F. Cheng and R. Johnson, in *Origin and Evolution of Planetary and Satellite Atmospheres*, S. Atreya, J. B. Pollack, M. Matthews, Eds. (Univ. of Arizona Press, Tucson, 1989), p. 682.
22. S. M. Krimigis *et al.*, *Planet Space Sci.* **36**, 311 (1988).
23. A. L. Broadfoot *et al.*, *Science* **233**, 74 (1986).
24. L. J. Lanzerotti, *Nucl. Instrum. Methods* **B32**, 412 (1988).
25. A. F. Cheng *et al.*, in *Satellites*, J. A. Burns and M. Matthews, Eds. (Univ. of Arizona Press, Tucson, 1986), p. 403.
26. L. J. Lanzerotti *et al.*, *J. Geophys. Res.* **92**, 14949 (1987).
27. M. L. Delitsky and W. R. Thompson, *Icarus* **70**, 354 (1987); W. R. Thompson, *Geophys. Res. Lett.* **16**, 969 (1989); W. R. Thompson *et al.*, *ibid.*, in press.

28. We thank the members of the Voyager project and personnel at the Jet Propulsion Laboratory and the Planetary Programs Office, NASA Headquarters, for help and cooperation in carrying out this experiment. We thank R. B. Decker, C. Paranicas, M. Kane, B. J. Hook, J. G. Gunther, and J. Green for their enthusiasm and long hours in support of the LECP Voyager project. The help of E. Miner, P. deVries, and O. Divers (among many others) was essential to the success of our investigation. We are also grateful to J. Belcher, D. Gurnett, N. Ness, and E. Stone for discussions concerning the interpretation of the data. The work at The Johns Hopkins University Applied Physics Laboratory was supported by NASA under Task I of Contract N00039-89-C-5301, N00039-89-C-0001, and by subcontracts at the Universities of Kansas and Maryland.

31 October 1989; accepted 15 November 1989

Energetic Charged Particles in the Magnetosphere of Neptune

E. C. Stone, A. C. Cummings, M. D. Looper, R. S. Selesnick, N. Lal, F. B. McDonald, J. H. Trainor, D. L. Chenette

The Voyager 2 cosmic ray system (CRS) measured significant fluxes of energetic [≳1 megaelectron volt (MeV)] trapped electrons and protons in the magnetosphere of Neptune. The intensities are maximum near a magnetic *L* shell of 7, decreasing closer to the planet because of absorption by satellites and rings. In the region of the inner satellites of Neptune, the radiation belts have a complicated structure, which provides some constraints on the magnetic field geometry of the inner magnetosphere. Electron phase-space densities have a positive radial gradient, indicating that they diffuse inward from a source in the outer magnetosphere. Electron spectra from 1 to 5 MeV are generally well represented by power laws with indices near 6, which harden in the region of peak flux to power law indices of 4 to 5. Protons have significantly lower fluxes than electrons throughout the magnetosphere, with large anisotropies due to radial intensity gradients. The radiation belts resemble those of Uranus to the extent allowed by the different locations of the satellites, which limit the flux at each planet.

THE COSMIC RAY SYSTEM (CRS) measured significant fluxes of energetic electrons and protons stably trapped within the magnetosphere of Neptune during the close approach of Voyager 2 on 25 August 1989. The instrument consists of two high-energy telescopes (HETs), four low-energy telescopes (LETs), and an electron telescope (TET), each containing several solid-state detectors designed for the study of interplanetary cosmic rays (*1*). To allow for measurements over a large range of possible trapped particle intensities in the previously unknown environment of Neptune's magnetosphere, the instrument was cycled every 192 s between two configurations, and various anticoincidence requirements were disabled to prevent excessive deadtime effects. The instrument operated normally throughout the encounter, and none of the detectors was saturated by high particle fluxes.

The Voyager 2 trajectory past Neptune took the spacecraft over the north pole of the planet within 0.2 planetary radius (R_N = 24,765 km) of the cloud tops, by far the closest passage of any planetary encounter during the mission. Experience from the other giant planets led to the expectation of rapidly increasing fluxes of trapped radiation as the planet was approached. In addition, recent ground-based observations of radio emissions from Neptune suggested an intense radiation belt (*2*). Since Triton, at 14.3 R_N, was the closest satellite of Neptune known before the Voyager encounter, such an intense radiation belt seemed possible in the absence of satellite sweeping. In fact, the situation at Neptune is quite different from these expectations before the encounter, with the inner radiation belt being limited to relatively low intensity by satellite sweeping.

Electrons. The counting rate profiles in Fig. 1a, shown versus spacecraft event time (SCET), represent electron fluxes at energies greater than approximately 1, 2.5, and 5 MeV (*3*). The distance of Voyager 2 from Neptune is indicated at the top of the figure in units of R_N. The flux above 1 MeV began to rise above the cosmic ray background level just inside the orbit of Triton and increased sharply for a period of about an hour. At ~8 R_N it leveled off and began to fall to the relatively low values near the planet. The peak flux was observed at 5.5 R_N on the outbound leg of the trajectory. Clearly there is considerable spatial structure in the trapped electron flux, which apparently is controlled by the newly discovered satellites and rings within 5 R_N from Neptune. The largest satellite, 1989N1, has an orbit (at 4.75 R_N) and size similar to those of Miranda, the innermost moon of Uranus, which plays an important role in limiting the trapped radiation intensity at that planet.

Because trapped electrons are guided by the magnetic field, it is usual to organize the data by using the magnetic shell parameter, *L*. Figure 1b shows the spacecraft *L* versus time in the offset tilted dipole (OTD) model of the planetary magnetic field (*4, 5*), which incorporates a 46.8° tilt of the magnetic

E. C. Stone, A. C. Cummings, M. D. Looper, R. S. Selesnick, California Institute of Technology, Pasadena, CA 91125.
N. Lal, F. B. McDonald, J. H. Trainor, NASA Goddard Space Flight Center, Greenbelt, MD 20771.
D. L. Chenette, Lockheed Palo Alto Research Laboratory, Palo Alto, CA 94304.

dipole axis from the planetary rotation axis and a 0.55 R_N offset of the dipole from the center of the planet. The OTD model is not accurate inside 4 R_N, and the spacecraft OTD L in Fig. 1b is changed to a dotted line in that region. The dashed horizontal lines indicate two local minimum L values reached by each of the satellites Triton, 1989N1, and 1989N2. The satellite absorption efficiency is strongly peaked near the minimum L (*6*). There are two dashed lines for each satellite because there is a component of the dipole offset that is perpendicular to the dipole axis, so that during each planetary rotation the satellite reaches two local minimum L values, which alternate between the values shown. In addition to the satellites shown, there are four small satellites and three rings in the radial distance range between 2 and 3 R_N. We have also indicated (Fig. 1b, dashed and dash-dot curves) two possible modifications to the spacecraft L which, if valid in the multipole field, provide sensible interpretations of the variations in the electron counting rates. The labels in Fig. 1, a and b, indicate features that are discussed below. The spacecraft trajectory in a coordinate system that is fixed in the reference frame of the OTD magnetic field is shown in Fig. 2. The Z axis is parallel to the OTD dipole axis, and the R axis is the cylindrical distance from the dipole axis. Again, the trajectory is shown by a dotted line inside 4 R_N, and the dashed dipole field lines correspond to the satellite local minimum L values shown in Fig. 1b.

The data in Fig. 1a show variations which, if due to satellite absorption, should be understood by comparing the spacecraft L with the minimum L values of the satellites. According to the OTD model, the Triton minimum L region was crossed twice in the outer magnetosphere, near 2320 on day 236 (labeled A in Fig. 1, a and b) and 0855 on day 237 (K) (all times are in SCET). In each case the flux of $\gtrsim 1$ MeV electrons rose above background just inside the Triton minimum L, perhaps the result of absorption by Triton. This observation is consistent with the predictions of the OTD model but does not provide a critical test because, on account of the background level, an unambiguous signature of Triton was not observed. The OTD model does not predict any further encounters with the Triton minimum L until inside a radial distance of 3 R_N, where the OTD model is not an accurate representation of the observed field. However, in the absence of higher order multipoles the OTD model would predict two crossings of the Triton minimum L region at 0320 (C) and 0350 (D). In the first case (C) the flux was at least 100 times that observed near the same OTD L in the outer magnetosphere (A or K) and was near a peak in the flux, rather than a minimum as expected for satellite absorption. In the second case (D) the flux was at least ten times higher than observed in the outer magnetosphere and was in a region of rapidly decreasing flux. These observations imply that, not unexpectedly, the OTD model does not provide an accurate representation of the L shells inside 3 R_N. In addition, significant trapped fluxes were observed at 0330, at which time the OTD model predicts an absence of trapped particles because of a polar cap passage.

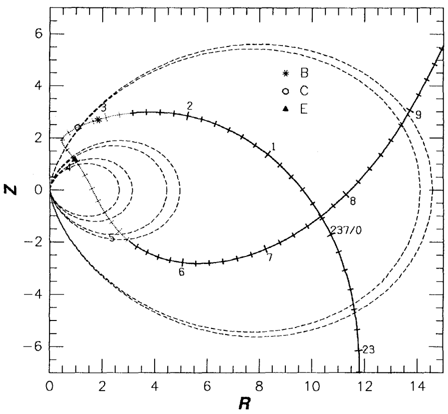

Fig. 2. Trajectory of Voyager 2 projected into a magnetic meridional plane. The Z axis is parallel to the OTD dipole axis, and the R axis represents the cylindrical distance from the dipole axis. The trajectory is shown by a dotted curve inside 4 R_N. The time tick marks along the trajectory are at 10-min intervals and labeled at the beginning of each hour in SCET. The dashed pairs of dipole field lines are the two local minimum L values of the satellites 1989N2, 1989N1, and Triton (in order of increasing L). The symbols labeled B, C, and E correspond to similarly labeled features in Fig. 1.

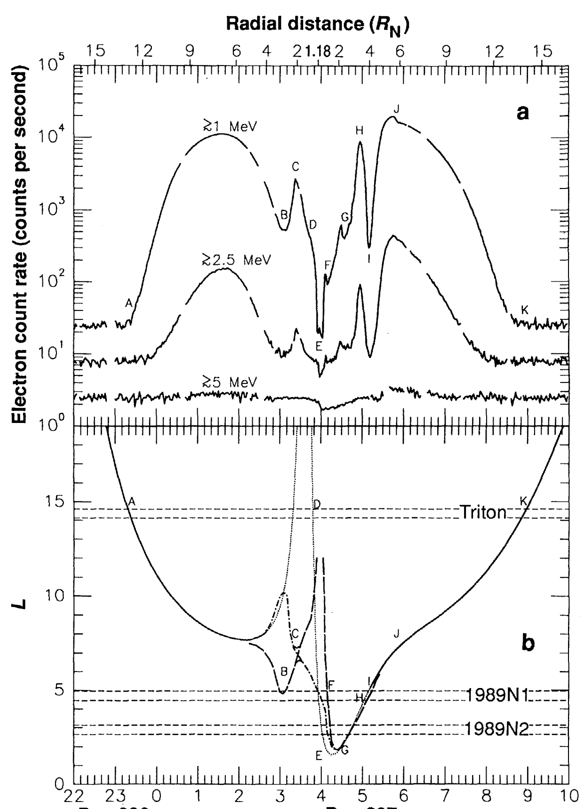

Fig. 1. (**a**) Counting rate profiles for electrons with kinetic energies greater than approximately 1, 2.5 (×0.3), and 5 MeV (×0.1) versus spacecraft event time (SCET). The corresponding radial distance of Voyager 2 from Neptune is labeled at the top in R_N (24,765 km). There was a mode change from 0250 to 0510 on day 237, which caused the statistical fluctuations in the $\gtrsim 5$ MeV rate to decrease during that period. The letters label features that are discussed in the text. (**b**) The solid curve, changing to a dotted curve inside 4 R_N, is the spacecraft L shell parameter versus SCET for the OTD magnetic field model. The dashed and dash-dot curves are estimates of two possible modifications to L, due to the nondipolar component of the magnetic field, which provide plausible interpretations of the features observed in the electron counting rates (a) as discussed in the text. The horizontal dashed lines indicate the two local minimum L values reached by the labeled satellites in the OTD model. The letters are centered at the same times as those in (a) (except for D and F, which are displaced ~5 min to the right) and label the features at those times.

The flux minimum at 0305 (B) was at a radial distance of about 3 R_N, closer to Neptune than the OTD model should be applied (*4*). Indeed, the OTD model predicts that the spacecraft L and magnetic latitude were increasing during the interval between the minimum L values of 1989N1 and Triton (see Fig. 2). Because this increase would not result in a flux minimum, two possible explanations have been considered. The minimum may be due to absorption by 1989N1, in which case the spacecraft L would have to be modified according to the dashed curve in Fig. 1b. Alternatively, the spacecraft may have reached a maximum L value in a region where the flux is a decreasing function of L, as indicated by the dash-dot curve in Fig. 1b. The OTD model does predict increasing values of L before the minimum flux (B), which may represent the highest L value reached by the spacecraft in the inner magnetosphere. A maximum spacecraft L at 0305 (B) must be less than the Triton minimum L, because the flux is considerably higher than that observed at the Triton minimum L in the outer magnetosphere (A or K). For the same reason, the flux minimum at 0305 (B) cannot be due to absorption by Triton.

There is a deep minimum in the $\gtrsim 1$ MeV electron flux at 0510 (I) just inside 4 R_N, where the OTD model should be valid. In fact, the minimum is close to the time that the spacecraft is predicted by the OTD model to have crossed the minimum L of 1989N1. The slight modification necessary to place the minimum flux at the average of the two 1989N1 minimum L locations is shown by the dashed curve in Fig. 1b. However, the OTD model predicts that absorption by 1989N1 should produce two local flux minima, separated in time by ~ 8 min, because of the two distinct local minimum L values of the satellite. It may be possible that the two minima are merged into one by radial diffusion, but a detailed calculation is required to determine whether the flux minimum could maintain its observed depth. Alternatively, if the component of the dipole offset perpendicular to the dipole axis is small enough to be neglected, then there is only one minimum L for each satellite, consistent with a single, deep flux minimum. Since the dipole offset in the OTD model is predominantly along the dipole axis, it would seem worthwhile to explore how well the observed magnetic field could be fit by a model with a smaller offset perpendicular to the dipole axis.

The low fluxes between the two peaks C and H all occurred within a radial distance of about 3 R_N. After the peak C, the flux falls rapidly to below the nominal cosmic ray background level, indicating an absence of trapped electrons. The lowest fluxes, from 0356 to 0403 (E), immediately followed the closest approach to Neptune, where the cosmic ray intensity is probably reduced by the proximity of the planet. Between 0355 and 0410 the spacecraft passed through the OTD minimum L values of all of the inner satellites and rings, suggesting that low flux at E may be due to absorption by all of these bodies. However, for reasons discussed below, two other possible interpretations are indicated in Fig. 1b. One alternative (the dashed curve) is a high-latitude return, in the polar cap region, to magnetic field lines that extend beyond the stable trapping limit. Because the absence of trapped particles occurred about 20 min later than the polar cap passage predicted by the OTD model, such an interpretation would require an uncomfortably large ($\sim 40°$) latitudinal shift of the polar cap boundary due to the distortion of the dipole field. Furthermore, it is not a priori likely that an observation of the polar cap would be located almost exactly at closest approach.

In the second alternative (dash-dot curve) the low-flux region (E), which occurred within 1.25 R_N, is simply a result of the spacecraft's passing below the radiation belts through a region resulting from atmospheric shadow effect. Such an atmospheric shadow is most likely to be observed near closest approach. Because of the complicated magnetic field geometry, the intersection of any given drift shell with the surface of the planet does not occur at a constant value of magnetic field magnitude, and particles that mirror at magnetic field intensities greater than the minimum surface field on that drift shell would be lost because of atmospheric absorption. Therefore, if the magnetic field at the spacecraft is larger than the surface magnetic field anywhere on the same drift shell, no trapped particles would be observed. The OTD magnetic field at the spacecraft near closest approach was about 0.065 G while the minimum OTD surface field on the same drift shell is less than 0.06 G, so the OTD model does predict an absence of trapped particles in this region. The observed magnetic field at closest approach was about 0.09 G (*4*), considerably larger than the OTD prediction, adding further to the plausibility of the spacecraft being below the trapped radiation at closest approach. Although satellite absorption cannot be ruled out, it is quite sensitive to the magnetic field near the planet, whereas the atmospheric shadow effect is likely for any sufficiently complex magnetic field. The two alternatives represented by the dashed and dash-dot curves in Fig. 1b may be interchanged at the point where they cross over, so, for example, the flux minimum at B may be due to 1989N1 (dashed curve), whereas the dropout at E may be due to an atmospheric shadow (dash-dot curve).

After the low-flux region (E), the flux increased rapidly until the small decrease, F. In the polar cap interpretation (dashed curve in Fig. 1b), this decrease would be due to the inbound crossing of the minimum L values of all of the newly discovered inner satellites, and the small maximum just earlier (0405) corresponds to the entire high-flux region between $L \approx 6$ and $L \approx 13$. In the atmospheric shadow interpretation (dash-dot curve in Fig. 1b), the 1989N1 minimum L may occur inside the low-flux region (E), in which case the small peak between the minima at E and F would be between 1989N2 and 1989N1 and on the same L shell as the peak H. When the spacecraft reached its minimum L of less than 2 (between F and G) the flux remained low, even though it was near the magnetic equator. The region G contains a great deal of structure attributable to the outbound crossing of the inner satellite L shells and is discussed in detail below. Because the spacecraft was at that time rapidly crossing L shells, the maximum flux near 0500 (H) must be inside the minimum L of 1989N1, the subsequent deep minimum (I) being due to absorption by that satellite. The broad maximum near 0600 is then an outbound passage through the maximum intensity region at $L \approx 7$. The

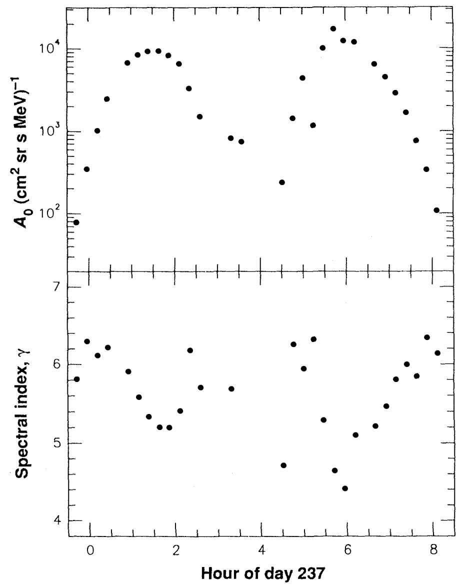

Fig. 3. Coefficient A_0, and the power law index, γ, versus SCET for an electron differential intensity spectrum of the form $A_0E^{-\gamma}$ in the energy range from 0.8 to 2.5 MeV. These were obtained from a fit to 15-min averages of the data represented by the upper two curves of Fig. 1 and pulse height–analyzed data from the $\gtrsim$1-MeV detector. The coefficient A_0 is described in units of (cm^2 sr s MeV)$^{-1}$ with E in MeV.

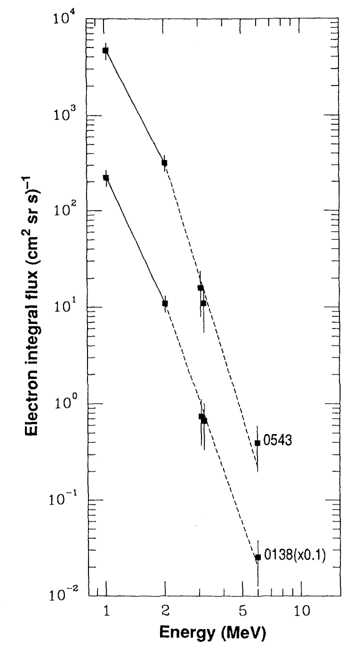

Fig. 4. Selected electron integral flux spectra for 15-min intervals centered at the indicated times (SCET). The two lowest energy points come from the results shown in Fig. 2. The spectrum at 0138 is multiplied by 0.1.

small dip near the peak at 0600 (J) is due to a spacecraft roll maneuver and shows that there is some anisotropy in the local pitch angle distribution.

We note that the observations in Fig. 1a outside ~2 R_N are consistent with a centered dipole magnetic field whose dipole axis is tilted by 34° from the rotation axis, if we assume that the flux minimum at B is due to 1989N1. This may be indicative of the type of distortion of the actual dipole magnetic field caused by the multiple field within ~4 R_N of the planet.

Electron spectra and sources. The upper two counting rate profiles in Fig. 1a can be used to estimate an electron energy spectrum from 1 to 2.5 MeV. The two detectors have been calibrated for this purpose, and their response functions are quite well known. Each has a wide angular acceptance, so that the ratio of the two counting rates is sensitive to the energy dependence of the spectrum and relatively insensitive to the pitch angle dependence. In addition, the ≳1 MeV rate is supplemented by pulse height analyzed events, which are binned into energy channels and provide more detailed information on the energy spectrum. The pulse height data were unavailable between 0255 and 0510, during which period only the counting rates were used. The spectra in the 1- to 2.5-MeV range are generally well represented by power laws in energy. The power law index and coefficient for the differential intensity spectrum as a function of time, on the basis of a maximum likelihood fit to the data, are shown in Fig. 3. An isotropic distribution has been assumed throughout. The electron spectra are generally soft with power law indices near 6, but the large-scale trends in the figure are significant, indicating somewhat harder spectra in the regions of peak flux.

Two electron integral flux spectra are shown in Fig. 4. The indicated times refer to the centers of 15-min periods over which the data were averaged. The two lowest energy points, at 1 and 2 MeV, were obtained from the power law fits described above. The higher energy points were obtained from estimates of the high-energy detector efficiencies based on the thickness of passive shielding surrounding each detector (*3*). Again, we assume that the distribution function is isotropic. The error bars represent systematic uncertainties, which are much larger than statistical errors. These results show some indication of the spectra softening at energies above 2 MeV (the changes in power law index are ~1 and 2.5 for the spectra at 0138 and 0543, respectively).

Ground-based radio observations before the Voyager encounter (*2*) attributed an

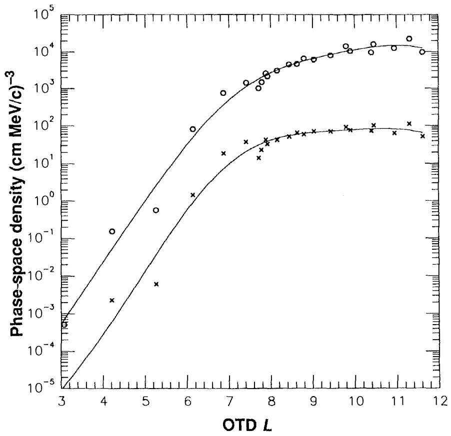

Fig. 5. Phase space density versus L for electrons confined to the magnetic equator with magnetic moments of 9000 (open circles) and 24,000 (crosses) MeV/G. The curves are smoothed versions of the data. Data points inside $L \approx 7$ are taken only from the outbound portion of the trajectory where the OTD model is approximately valid (see Fig. 1b).

excess emission at 20 cm to synchrotron radiation by a high flux of ~20-MeV electrons close to Neptune. A model calculation (*2*) of the integral flux of electrons >20 MeV required to produce the reported radio emission gave ~10^6 (cm^2 sr s)$^{-1}$ at L = 2, corresponding approximately to the magnetic equator crossing near 0420 (Fig. 2). The observed integral flux of electrons >5 MeV was everywhere less than 1 (cm^2 sr s)$^{-1}$ (Fig. 4), which provides a very conservative upper limit on the >20-MeV flux.

In addition, the magnetic field near the planet (~0.1 G) is lower than the 1-G value used in interpreting the ground-based data, which further reduces the flux of synchrotron radiation. Based on these comparisons, we conclude that the excess radio flux at 20 cm could not have been due to synchrotron radiation.

From the results in Fig. 3 we have made initial estimates of the radial dependence of the phase space density, $f = j/p^2$, for equatorially confined electrons, where j is the differential intensity and p is the momentum. The results are shown in Fig. 5 as a function of L for two values of the first adiabatic invariant, $M = p^2/2mB_0$, where m is the electron rest mass, and $B_0 = 0.13/L^3$ G is the equatorial magnetic field. In radial diffusion M is conserved. The large positive radial gradient between $L \approx 3$ and $L \approx 8$ is not sensitive to the assumption of an isotropic distribution and indicates that electrons diffuse inward from a source in the outer magnetosphere.

Protons. Proton data as a function of SCET for two energy ranges are shown in Fig. 6. The data points represent the flux of 3.2- to 5-MeV protons averaged over 30-min bins and are derived from a three-parameter pulse height analysis. The two different symbols correspond to measurements from identical LETs (LET C and LET D) separated by a 90° angle with 25° acceptance cone half-angles, and therefore provide a local measure of anisotropy. The counting rate profile (small points) is a fourfold coincidence, which, for galactic cosmic rays, responds primarily to protons at energies of 63 to 160 MeV and to helium nuclei at energies >70 MeV per nucleon (*3*); the latter dominates the nominal response.

Significant fluxes of 3.2- to 5-MeV protons were observed inside $L \approx 10$. This result is similar to that obtained at Uranus (*7*) and is consistent with the stable trapping limit expected on the basis of the Stormer vertical cutoff rigidity (*8*). The peak flux, however, was a factor of ~10 higher than that observed at Uranus and occurred in the outer trapping region near L = 8. In contrast, the peak electron flux was about a factor of 10 lower than at Uranus. At Saturn the fourfold coincidence rate responded to a high proton flux in the inner magnetosphere from cosmic ray albedo neutron decay (CRAND) (*9*). At Neptune there is no

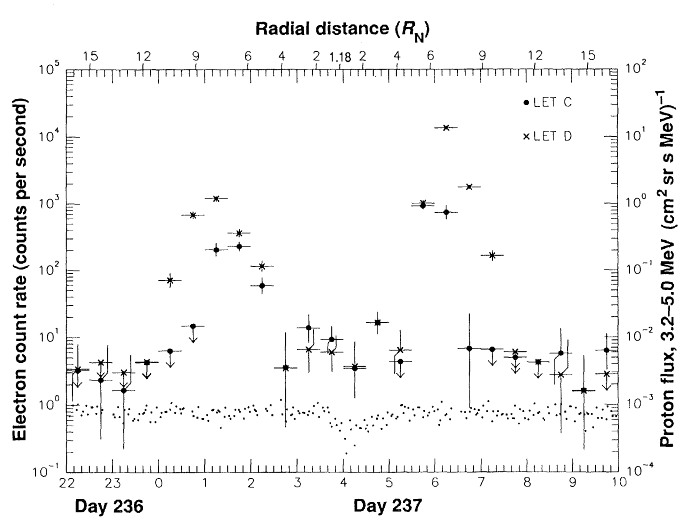

Fig. 6. Proton fluxes (right scale) and counting rates (left scale). The data points represent the flux between 3.2 and 5 MeV from LET C (solid circles) and LET D (crosses). The points with arrows are upper limits. The rate profile (small points) is a fourfold coincidence measurement for 63- to 160-MeV protons and ≳70-MeV/nucleon helium. The vertical error bars represent 1σ statistical uncertainties.

evidence for such a source. The Stormer cutoff for 63-MeV protons is near $L = 5$, which corresponds approximately to the depression in the flux from about 0330 to 0520 (see Fig. 1b), except near closest approach, where geometrical shadowing is effective. The asymmetry of the feature perhaps indicates a slower variation of L outbound.

Proton energy spectra are shown in Fig. 7 for the time period from 0100 to 0130 on day 237. Data are shown from the same two LETs as in Fig. 6 (LET C and LET D), which are separated by a 90° angle, and from LET A, which is oriented in the opposite direction to LET C. The protons appear to have a somewhat flatter spectrum than the electrons at low energies, steepening to a similar power law above 2 to 3 MeV. Directional anisotropies are clearly evident in both Figs. 6 and 7. These are largest in regions outside the peak flux, from $L \approx 7$ to $L \approx 10$, where the flux measured by LET D is considerably higher than that measured by LET C. The effect increases with energy (Fig. 7). These anisotropies are consistent, both in magnitude and direction, with those expected as a result of the radial intensity gradient. That is, LET C and LET D measure protons whose guiding centers are located one proton gyroradius from the spacecraft in regions of significantly different guiding center density.

Small satellite and ring absorption. When energetic charged particles trapped in the magnetosphere strike satellites or ring material in orbit about Neptune, the charged particles may be absorbed completely, or they may lose so much energy that they fall below the energy thresholds of the CRS detectors. Thus, orbiting satellites and ring material produce absorption signatures that are a kind of shadow of that material in the energetic particle flux (*10*). Because charged particles are directed by the magnetic field, these signatures or shadows are cast along the magnetic field line direction and eventually around the entire drift shell. The analysis of such signatures at Jupiter, Saturn, and Uranus has yielded important and unique information about the structure and dynamics of those magnetospheres.

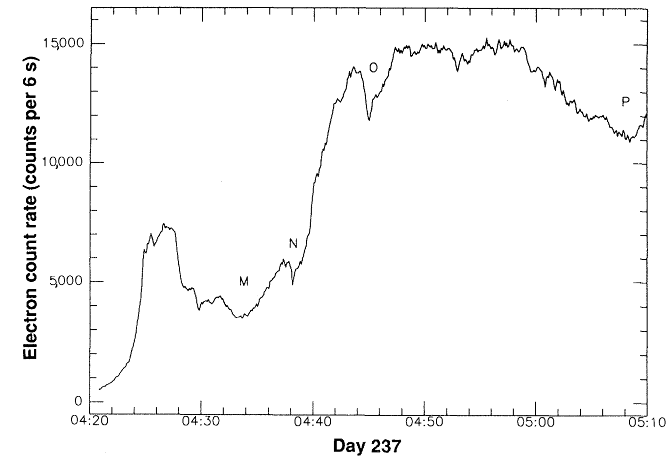

Fig. 8. Six-second samples of the CRS L1 counting rate from LET A, as a function of SCET, in the region of small satellite and ring absorption.

The close approach of Voyager 2 to Neptune provided an opportunity to observe the signatures of the several newly discovered rings and small satellites, which orbit between 2 and 3 R_N from the planet. We present observations of the energetic electron flux in this region during the time interval from 0425 to 0455 on day 237 (Fig. 8). These data, which provide the highest available time resolution, are from a LET detector that nominally responds to protons but in regions of high electron flux responds primarily to pileup of electrons with energies greater than 20 keV. Each data point is the number of counts in the 6-s accumulation time, so that statistical fluctuations occur with a standard deviation approximately equal to the square root of the value.

A broad decrease in flux from about 0428 to 0442 is shown in Fig. 8, superimposed on the general trend of increasing flux in this region. The decrease can also be seen in the $\gtrsim$1-MeV electron rate at G in Fig. 1a. From about 0444 to 0447 there is another significant decrease, and throughout the region there are flux decreases of varying width and depth that are well above the level of statistical fluctuations. After 0500 the flux drops continuously into the deep minimum associated with absorption by 1989N1.

From 0430 to 0500 the spacecraft L was increasing from ~2 to 4. The satellites and rings absorb charged particles at a rate that is strongly peaked near their minimum L values, where they spend the longest time. The minimum L is approximately the orbital radius of the body, so that Fig. 8 covers the region of maximum expected absorption for all of the inner satellites and rings. However, identification of the features in Fig. 8 with particular absorbers is complicated by their relative proximity and the complex magnetic field geometry. When the magnetic field is not azimuthally symmetric, the satellites will have multiple local minimum L values occurring at different phases in their orbits. For example, in the OTD magnetic field model the satellites (and rings) have two local minimum L values, associated with an approach to the magnetic equator when the dipole offset is either toward or away from the satellite. In the OTD model, we would therefore expect either two distinct absorption features from each satellite, or one broad one in the case that radial diffusion has caused the two to merge. The two minima are displaced inward and outward from the mean orbital radius by ~0.25 R_N. The major flux decrease in Fig. 8 contains distinct local minima and must be the result of absorption by several of the satellites and rings. However, the width of the local features is less than 0.5 R_N, and their spacing is on the order of 0.5 R_N. The interpretation of these features will therefore require further analysis and modeling of the absorption process in the complex magnetic field.

The interpretation of Fig. 8 is simplified considerably if, inside of 3 R_N, the azimuthal asymmetries relative to the dipole axis of the OTD model are small compared to the width of the observed absorption features ($\lesssim$0.2 R_N). Then the major satellite absorption regions would be well separated, leading to a unique ordering of the absorption features with radial distance. In this case, a

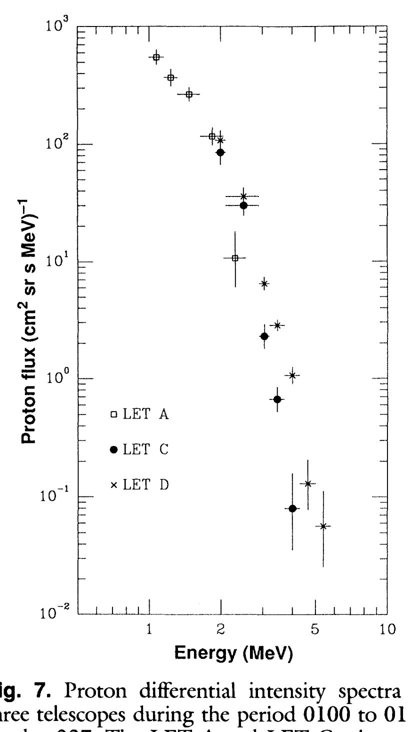

Fig. 7. Proton differential intensity spectra in three telescopes during the period 0100 to 0130 on day 237. The LET A and LET C telescopes point in opposite directions; the LET D telescope is oriented 90° from LET A and C. The vertical error bars represent 1σ statistical uncertainties.

tentative identification is possible for the four major absorption regions labeled in Fig. 8. The features M, N, and O would likely be due to absorption by 1989N3 and the 53k ring combined, 1989N4, and 1989N2, respectively, whereas the feature P corresponds to the 1989N1 signature labeled as I in Fig. 1a. Given that the features occur at L values equal to the orbital radii of the absorbers, a smooth variation of L with time is obtained and shown by the dashed curve in Fig. 1b for the time period from 0430 to 1510. More detailed comparisons will be required to evaluate the consistency of such an L dependence with the magnetic field observations.

REFERENCES AND NOTES

1. E. C. Stone *et al.*, *Space Sci. Rev.* **21**, 355 (1977).
2. I. de Pater and C. K. Goertz, *Geophys. Res. Lett.* **16**, 97 (1989).
3. Electron counting rates in Fig. 1a were obtained from the following detectors: D1 ($\gtrsim$1 MeV, $G \approx 11$ cm^2 sr, 6% duty cycle), D2 ($\gtrsim$2.5 MeV, 6% duty cycle), D4 ($\gtrsim$5 MeV, 6% duty cycle changing to 100% duty cycle between 0250 and 0510 on day 237). The three high-energy points in Fig. 4 were obtained from the following detectors: C2 (high gain, $\gtrsim$3.1 MeV, $G \approx 11.2$ cm^2 sr), C3 (high gain, $\gtrsim$6 MeV, $G \approx 42.4$ cm^2 sr), C4 (high gain, $\gtrsim$3.1 MeV, $G \approx 20.5$ cm^2 sr). The counting rate data in Fig. 6 are from B2, C4, C3, and C2 coincidence (low gain, 63- to 160-MeV protons and $\gtrsim$70 MeV/nucleon helium, $G \approx 11$ cm^2 sr, 50% duty cycle). See (*1*) for more information.
4. N. F. Ness *et al.*, *Science* **246**, 1473 (1989).
5. We define L in the OTD model as $r/\cos^2\lambda$, where r is the radial distance from the center of the offset magnetic dipole in R_N and λ is the magnetic latitude.
6. M. T. Paonessa and A. F. Cheng, *J. Geophys. Res.* **92**, 1160 (1987).
7. E. C. Stone *et al.*, *Science* **233**, 93 (1986).
8. J. R. Thomas and W. R. Doherty, *Jet Propulsion Laboratory Tech. Memo. 33–543* (1972), p. 315.
9. R. E. Vogt *et al.*, *Science* **215**, 577 (1982).
10. See, for example, J. A. Van Allen, M. F. Thomsen, B. A. Randall, *J. Geophys. Res.* **85**, 5709 (1980).

11. We thank R. E. Vogt for his contributions during his tenure as principal investigator for the CRS system on Voyager 2. We thank the Voyager project members and the enthusiastic staff of our laboratories at Caltech and Goddard Space Flight Center for their excellent support; special thanks go to P. Schuster, R. Kaiper, R. McGuire, T. Garrard, B. Gauld, R. Burrell, and O. Divers. Thanks also to P. Liggett, L. Lee, C. Byrne, S. Burleigh, and the rest of the VNESSA staff at the Jet Propulsion Laboratory. Supported by NASA under contracts NAS7-918 and NGR 05-002-160.

31 October 1989; accepted 15 November 1989

First Plasma Wave Observations at Neptune

D. A. Gurnett, W. S. Kurth, R. L. Poynter, L. J. Granroth, I. H. Cairns, W. M. Macek,* S. L. Moses, F. V. Coroniti, C. F. Kennel, D. D. Barbosa

The Voyager 2 plasma wave instrument detected many familiar plasma waves during the encounter with Neptune, including electron plasma oscillations in the solar wind upstream of the bow shock, electrostatic turbulence at the bow shock, and chorus, hiss, electron cyclotron waves, and upper hybrid resonance waves in the inner magnetosphere. Low-frequency radio emissions, believed to be generated by mode conversion from the upper hybrid resonance emissions, were also observed propagating outward in a disklike beam along the magnetic equatorial plane. At the two ring plane crossings many small micrometer-sized dust particles were detected striking the spacecraft. The maximum impact rates were about 280 impacts per second at the inbound ring plane crossing, and about 110 impacts per second at the outbound ring plane crossing. Most of the particles are concentrated in a dense disk, about 1000 kilometers thick, centered on the equatorial plane. However, a broader, more tenuous distribution also extends many tens of thousands of kilometers from the equatorial plane, including over the northern polar region.

The Voyager 2 flyby of Neptune on 25 August 1989 revealed that Neptune has a large and complex magnetosphere. In this report we present the first observations of plasma waves and low-frequency radio emissions in the vicinity of Neptune. The plasma wave (PWS) instrument on Voyager is designed to measure the electric field of plasma waves and radio emissions in the frequency range from 10 Hz to 56.2 kHz. Further information on this instrument is given by Scarf and Gurnett (*1*). To provide a framework for presenting the results, the observations are described approximately in the order in which the phenomena occurred, starting with low-frequency radio emissions detected during the approach to Neptune, and ending with observations during the outbound leg in the vicinity of Neptune's moon, Triton.

Radio emissions. Although the planetary radio astronomy instrument started to detect radio emissions at high frequencies (>100 kHz) as much as 30 days before closest approach (*2*), the plasma wave instrument did not detect radio emissions at low frequencies (<100 kHz) until only a few days before closest approach. Even then the intensities were very weak. The low-frequency radio emissions can be seen in the 5.62- through 56.2-kHz channels of Fig. 1, which shows an overview of the PWS electric field intensities during a 32-hour interval centered on closest approach. The radio emission intensities gradually increase as the spacecraft approaches the planet, reach a broad irregular peak around closest approach, and then gradually decrease as the spacecraft recedes from the planet. The low-frequency limit of the radio emission spectrum is about 5 kHz. At high frequencies the spectrum continues smoothly into the frequency range of the planetary radio astronomy instrument, with no evidence of a high-frequency cutoff. Wideband waveform measurements, which provide very high spectral resolution over the frequency range from 50 Hz to 12 kHz show that the spectrum is usually smooth and continuous, very similar to continuum radiation in Earth's magnetosphere (*3*). In a few cases, narrowband components can be seen with bandwidths of a few percent or less.

In addition to the radial distance dependence evident in Fig. 1, the radio emission intensity is also modulated by the rotation of the planet. This modulation pattern is difficult to analyze near closest approach because of the close proximity to the source and the rapid longitudinal motion of the spacecraft. The best measurements of the rotational modulation are obtained far from the planet, particularly on the outbound leg. The basic pattern is illustrated in Fig. 2, which shows the intensity variations in the 17.8-kHz channel from 27 to 30 August, at a radial distance of 140 to 315 Neptune radii (1 R_N = 24,762 km). The intensity scale in this plot has been expanded to show signals just above threshold. The modulation pattern consists of two bursts every 16 hours. The 16-hour period is consistent with the 16-hour rotation period determined by the planetary radio astronomy instrument (*2*). The two-pulse-per-rotation pattern is believed to arise from a disklike beaming geometry, with the plane of the disk tilted with

D. A. Gurnett, W. S. Kurth, L. J. Granroth, I. H. Cairns, W. M. Macek, Department of Physics and Astronomy, University of Iowa, Iowa City, IA 52242.
R. L. Poynter, Jet Propulsion Laboratory, 4800 Oak Grove Drive, Pasadena, CA 91109.
S. L. Moses, F. V. Coroniti, C. F. Kennel, TRW Space and Technology Group, One Space Park, Redondo Beach, CA 90278.
D. D. Barbosa, Institute of Geophysics and Planetary Physics, University of California, Los Angeles, Los Angeles, CA 90024.

*On leave from Space Research Center, Polish Academy of Sciences, Warsaw, Poland.